Journal of Power Sources 294 (2015) 1–7

Contents lists available at ScienceDirect

Journal of Power Sources

journal homepage: www.elsevier.com/locate/jpowsour

Facile synthesis of mesoporous V_2O_5 nanosheets with superior rate capability and excellent cycling stability for lithium ion batteries

Huanqiao Song [a, *], Cuiping Zhang [a], Yaguang Liu [a], Chaofeng Liu [a], Xihui Nan [a], Guozhong Cao [a, b, *]

[a] *Beijing Institute of Nanoenergy and Nanosystems, Chinese Academy of Sciences, Beijing 100083, China*
[b] *Department of Materials and Engineering, University of Washington, Seattle, WA 98195-2120, USA*

HIGHLIGHTS

- A new mesoporous V_2O_5 nanosheet cathode has been developed for Li-ion batteries.
- This V_2O_5 nanosheet cathode shows excellent rate capability and cyclic stability.
- The large surface area accelerates electrolyte penetration and Li-ion diffusion.
- Mixed-valence V^{4+}/V^{5+} results in a high electrical conductivity of V_2O_5 nanosheets.

ARTICLE INFO

Article history:
Received 26 March 2015
Received in revised form
25 April 2015
Accepted 10 June 2015
Available online 16 June 2015

Keywords:
Mesoporous V_2O_5 nanosheets
Oxygen vacancies
Large specific surface area
Electron/Li-ion transport
Stability and rate capability

ABSTRACT

A facile synthesis of mesoporous V_2O_5 nanosheets has been developed by a simple hydrothermal method and subsequent instantaneous heating and calcination. These V_2O_5 nanosheets exhibit ultrastable capacity retention at different current density, and also show excellent rate capability, maintaining a reversible capacity of 118 mA h g^{-1} at 6000 mA g^{-1} after 1000 cycles. The remarkable performance results from their unique mesoporous nanosheet structure as well as the presence of noticeable amount of tetravalent vanadium ions and the attendant oxygen vacancies in V_2O_5, which have substantially improved electronic-ionic transport and mitigated the internal mechanical stress induced by the volume variation of the material upon cycling. These results demonstrate the significant potential of mesoporous V_2O_5 nanosheets for high power and long life batteries. Moreover, the simple and general synthesis method is suitable for the preparation of a variety of electrode material with unique mesoporous nanostructure containing oxygen vacancies for electrochemical batteries and supercapacitors.

1. Introduction

Lithium ion batteries (LIBs) are always considered as the most promising and widely used rechargeable batteries, because they are efficient in energy conversion and storage and have the advantages of light weight, high working voltage and capacity, long cycling life and environmentally benign [1–5]. However, the energy density and power density of LIBs lag far behind the rapidly increasing demands of ever advancing electronic devices. The increase of energy density for LIBs requires the development of cathode materials with larger capacities and/or higher working voltages [6]. A further increase in capacity of the cathode will generally require multi-Li ion insertion and extraction reaction. However, the current studied cathode materials can only reversibly accept one Li ion and therefore deliver capacities lower than 200 mA h g^{-1} [7–11]. Vanadium pentoxide (V_2O_5), a typical intercalation compound, can accept multi-Li ion reversibly due to its special layer structure and the weak van der Waals forces that hold the layers together [12]. The different degree of Li intercalation (x) corresponds to the various phase transitions, for example α, ε, δ, γ, and ω phase corresponding to $x < 0.01$, $0.35 < x < 0.7$, $0.7 < x < 1$, $1 < x < 2$, and $2 < x < 3$ in $Li_xV_2O_5$ [12,13]. The theoretical capacity of V_2O_5 with two Li insertion/extraction is about 294 mA h g^{-1}, which is more than twice the commercial cathode materials, such as $LiCoO_2$ (140 mA h g^{-1}) and $LiMn_2O_4$ (148 mA h g^{-1}) [14–16]. Even only one

---

* Corresponding authors. Beijing Institute of Nanoenergy and Nanosystems, Chinese Academy of Sciences, Beijing 100083, China.
E-mail addresses: songhuanqiao@binn.cas.cn (H. Song), gzcao@u.washington.edu (G. Cao).

http://dx.doi.org/10.1016/j.jpowsour.2015.06.055
0378-7753/

Li insertion/extraction, the theoretical capacity of V_2O_5 (147 mA h g^{-1}) is also comparable to the common cathode material. However, V_2O_5 as cathode of LIBs still suffers low Li ion diffusion coefficient (10^{-12}–10^{-13} cm^2 s^{-1}), poor structure stability, and relatively low electronic conductivity (10^{-7}–10^{-6} S cm^{-1}) [17–21], which results in limited rate capability and long-term cycling stability. Many efforts have been made to overcome the limitations [13,22,23]. A major strategy is to fabricate the nanostructured V_2O_5 to mitigate against the slow electrochemical kinetics by introducing large surface area and short ion diffusion paths. For example, Leaf-like V_2O_5 nanosheets with a large Brunauer–Emmett–Teller (BET) specific surface area of 28 m^2 g^{-1} show very high rate capacity of 303 and 104 mA h g^{-1} at current density of 50 and 5000 mA g^{-1} between the voltage range of 2.0–4.0 V [23]. Mesoporous single-crystalline V_2O_5 nanorods assembled into hollow microspheres delivered a very high reversible capacity of 145.8 mA h g^{-1} at 0.5 C with much improved capability retention even at a rate of 50 C (101.6 mA h g^{-1}) at 2.5–4.0 V [24]. Various nanostructures reported with different performances indicate that the morphology and structure are critically important for the electrochemical performance of V_2O_5 cathode. And different V_2O_5 nanostructrues, such as one-dimensional nanotubes/wires/rods, two-dimensional (2 D) nanosheets and three-dimensional nanospheres, can effectively improve the electrochemical kinetics, shorten Li-ion diffusion distance and buffer the volume change, thus lead to higher capacity and chemical stability over many discharge/charge cycles as compared with non-nanostructured V_2O_5 [25–29]. Recently a series of V_2O_5 ultrathin nanosheets have been extensively reported with high specific capacities as cathode for LIBs [23,27,30]. However, it is worth noting that some nanosheets suffer from the poor cycling stability due to the decrease of intrinsic electronic conductivity or crystal structural fracture during the discharge/charge process. As is well known, mesoporous nanomaterial with large specific surface area exhibit great advantages such as good contact with the electrolyte, facile Li ion transport and improved binding between the nanostructures, which can reduce the structure stress during the Li insertion/extraction processes and decrease the polarization [24,31–34]. Thus, constructing the mesoporous V_2O_5 nanosheet with large specific surface area and improved electronic conductivity has been considered to be a valid way to improve Li ion transport and cycling stability of V_2O_5 cathode.

Herein, we demonstrate a novel and generic green method to prepare mesoporous V_2O_5 nanosheets as illustrated in Fig. 1. NH_3VO_3 was reacted with oxalic acid dihydrate by hydrothermal reaction at 180 °C to synthesize ultrathin $NH_4V_4O_{10}$ nanosheets. Then the $NH_4V_4O_{10}$ nanosheets were instantaneously heated and calcined at 400 °C in air to obtain mesoporous V_2O_5 nanosheets. This process is simple and can be scaled up to yield large quantities of mesoporous nanosheets. Used as cathode material for LIBs, these mesoporous V_2O_5 nanosheets exhibit excellent reversible Li storage properties, as lithium insertion in them is mainly surface Li storage with extremely short lithium diffusion lengths, thus can meet the requirement of the exceeding fast and stable lithium insertion/extraction processes.

2. Experimental section

2.1. Material preparation

All the starting materials were of analytically pure grade and used directly without any purification. mesoporous V_2O_5 nanosheets were prepared in two steps. First, 1.7 g ammonium metavanadate (NH_4VO_3, ≥99.0%, Sinopharm Chemical Reagent Co., Ltd.) and 1.82 g oxalic acid dihydrate ($C_2H_2O_42H_2O$, ≥99.5%, Sinopharm Chemical Reagent Co., Ltd.) were dissolved in 65 ml distilled water in sequence under room temperature with constant stirring for 12 h and dark red solution was obtained. Afterward, the solution, exhibiting a PH of ~2.5, was transferred into 100 ml Teflon lined autoclave and kept at 180 °C for 24 h $NH_4V_4O_{10}$ nanosheets were finally collected by centrifugation and washed three times with distilled water. After dried at 80 °C overnight, the collected powder was then immediately put into a 400 °C muffle furnace and maintain for 1 h and the mesoporous V_2O_5 nanosheets were obtained. To understand the formation mechanism of $NH_4V_4O_{10}$ nanosheets, time-dependent and oxalic acid-dependent experiments were carried out. The intermediates with reaction time of 0, 0.5, 2, 10 and 48 h and with oxalic acid of 0.92, 1.22, 1.52, 2.12 and 2.52 g were prepared with a similar approach, respectively. For comparison, V_2O_5 nanoparticle aggregates were also prepared by calcining NH_4VO_3 at 400 °C for 1 h using the same heating process.

2.2. Material characterization

XRD was performed on a Bruker powder diffraction system (model D8 Advanced) with a Cu Ka radiation source. Different 2θ angular regions were investigated at a scan rate of 6° min^{-1} with a step of 0.02°. XPS analysis was conducted on a K-Alpha 1063 instrument with monochromated Al-Ka as the X-ray source. Charging effects were corrected by adjusting the binding energy of C 1s to 284.6 eV in the XPS spectra. A non-linear, least-squares algorithm was employed to determine the best fit to each of the V 2P core level spectra with two Gaussian–Lorentzian curves corresponding to two oxidation states (V^{4+} and V^{5+}). The relative atomic ratio of V^{4+} and V^{5+} was determined from the respective area ratios of these fits. The elemental composition of mesoporous V_2O_5 nanosheets was determined using an energy dispersive X-ray spectrometer (EDS OXFORD INCA 300).

The morphologies of the as-prepared composite materials were detected by field emission scanning electron microscope (FE-SEM, SU 8020) at 10 kV. TEM investigations were performed using a JEOL JEM-2010 instrument with an accelerating voltage of 200 kV. The thickness and width of nanosheets were determined by atom force microscopy (AFM, MFP-3D-SA-DV). N_2 adsorption–desorption analysis was carried out using a Micromeritics ASAP 2020 HD88. The typical sample weight used was about 200 mg. The outgas

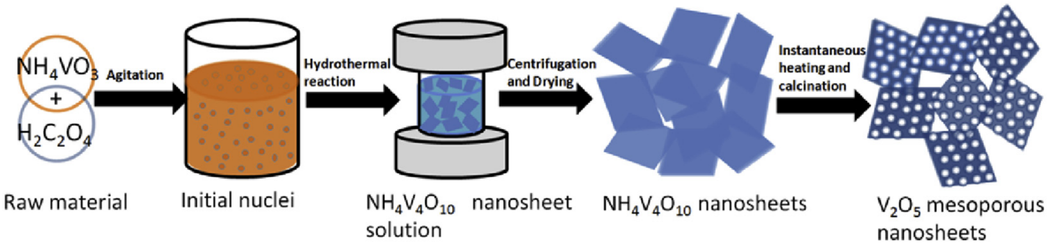

Fig. 1. Schematic illustration of the synthesis route of V_2O_5 mesoporous nanosheets in this work.

condition was set to 240 min at 250 °C under vacuum, and all adsorption–desorption measurements were carried out at liquid nitrogen temperature.

2.3. Electrochemical measurements

The working electrode was prepared by mixing the active material, polyvinylidene fluoride, and Super P conductive carbon in the weight ratio of 70: 10: 20. N-methylpyrrolidone was used as the solvent. The resultant slurry was then uniformly spread onto Al foil current collector and dried overnight at 80 °C. After solvent evaporation and heating at 120 °C in a vacuum oven for 12 h, the electrodes were cut into disks and assembled into CR2025 coin type cells in a glove box filled with pure argon. Celgard polypropylene was used as the separator. The electrolyte was 1.0 M $LiPF_6$ in a mixture of ethylene carbonate and dimethyl carbonate (1:1). Li metal was used as the counter electrode and reference electrode. The mass density of the active material in each electrode disk is 2.5–3.5 mg cm^{-2}. The electrochemical performances of the prepared electrodes were characterized with a Land CT2001A tester system at room temperature. The cells were galvanostatically discharged and charged at different current density within the range of 2.5–4.0 V (*vs.* Li/Li^+). Cyclic voltammetry (CV) tests were carried out using Solartron electrochemical workstation at room temperature at a scan rate of 0.2 mV s^{-1} in the voltage range of 2.5–4.0 V (*vs.* Li/Li^+). The specific capacity and the current density were calculated based on the mass of active material. Electrochemical impedance spectroscopy (EIS) experiments were performed using the Solartron 1287A in conjunction with a Solartron 1260A impedance analyzer over the frequency range from 100 kHz to 0.01 Hz and the AC amplitude was 10.0 mV. Before the EIS test, the cells were charged fully and then kept for a period of time to reach a stable state. The electrical conductivities of the prepared samples were measured by the direct current (DC) four-probe technique, as described elsewhere [35,36]. The sample was made into a pellet at a pressure of 100 MPa, and then the pellet was gold coated, dried and sandwiched between stainless steel blocking electrodes for electrical conductivity measurements.

3. Results and discussion

The crystal phase of $NH_4V_4O_{10}$ nanosheet is first confirmed by its X-ray diffraction pattern, as shown in Fig. 2a, which demonstrates that all the reflections of the samples are in good agreement with the standard pattern of the pure monoclinic $NH_4V_4O_{10}$ phase (JCPDS No. 31–0075). No other impurities are detected in the patterns. The morphologies of the sample are then studied by field-emission scanning electron microscopy (FESEM) and transmission electron microscopy (TEM). As shown in Fig. 2b, the as prepared $NH_4V_4O_{10}$ precursor consists of discrete and uniform nanosheets with the width of around 250 nm. The magnified FESEM images (Fig. 2c) further reveal that the samples are composed of nanosheets with a thickness of about 20 nm, which is in agreement with the atom force microscopy (AFM) result and the corresponding height profiles in Fig. S2a. The TEM image in Fig. 2d shows the stacking layer structure of $NH_4V_4O_{10}$ nanosheet and the corresponding selected area electron diffraction (SAED) shows that the nanosheet crystal is a single crystal and the diffraction spot can be indexed to monoclinic $NH_4V_4O_{10}$ structure, which is consistent with the XRD result. The high resolution (HR)TEM image (Fig. 2e) taken from the edge of the nanosheet presents the clear lattice fringes with spacings of 0.35 nm and 0.32 nm which can be indexed to the (110) and (111) planes of monoclinic $NH_4V_4O_{10}$, respectively. The mechanism for the formation of this 2D $NH_4V_4O_{10}$ nanosheet can be described as follows based on the hydrothermal reaction:

$$8NH_4VO_3 + H_2C_2O_4 \xrightarrow{180^{\circ}C} 2NH_4V_4O_{10} + 2CO_2\uparrow + 4H_2O + 6NH_3\uparrow \tag{1}$$

During the process, $NH_4V_4O_{10}\cdot nH_2O$ firstly form in the reaction solution due to the reduction of oxalic acid, so the phase of amorphous $NH_4V_4O_{10}$ can be observed in the XRD pattern of the intermediates before hydrothermal reaction (Fig. S3, 0 h). The crystal structure of $NH_4V_4O_{10}\cdot nH_2O$ has been proved to be similar to that of $V_2O_5\cdot nH_2O$ in literature [37–40], which is composed of double layers of V_2O_5 stacked along the c-axis of a monoclinic unit cell and separated by water molecules and ammonium ions. Therefore, the $NH_4V_4O_{10}\cdot nH_2O$ consist of anisotropic ribbon-like nanofibers (60 nm wide and some μm in length) in Fig. 3b as hydrous V_2O_5 did in literature [23,41–43], when the hydrothermal reaction was carried out for 0.5 h. However, as reported by Trikalitis et al. [37], when the vanadium atoms centering the octahedral unit become reduced (from V^{5+} to V^{4+}) their radius increases and the V=O bond lengthens, leading to a less distorted VO_6 octahedron. The lengthening of the V=O bonds is mainly due to the d orbital of V^{5+} is predominantly antibonding in character and tend to reduce the bond order when populated with electrons to form V^{4+}. The weaker bonds within the intercalated $[V_2O_5]^{X-}$ framework, coupled with the increased disorder and decreased coherence length, result in the bigger mechanical brittleness of the redox intercalated V_2O_5 material. Therefore, some shorter nanorods (broken nanoribbons) were seen besides the nanoribbons in Fig. 3b. Moreover, although there is no vanadium-water coordination in $NH_4V_4O_{10}$ xerogel, it still could occur at the edges of the nanoribbons, which leads to the observed more dispersed nanoribbons [44]. Then the nanorods or nanoribbons in solution grow together along specific crystal facets to form single crystal $NH_4V_4O_{10}$ nanosheets (Fig. 3c) through Ostwald ripening [45]. The small nanosheets agglomerate and grow up and the large nanosheets are torn and broken in the condition of hydrothermal reaction (Fig. 3d). With the reaction going on, all the nanorods or nanoribbons are transformed into well-developed uniform intermediate nanosheets. Then several nanosheets stack homoepitaxially over one another to minimize the system energy, leading to $NH_4V_4O_{10}$ superstructure formation while preventing fusion between individual nanosheets in Fig. 3e. It is also worthy noted that there are significant effects of oxalic acid concentration on the final structure. A lower or higher concentration of oxalic acid in the starting solution could lead to diminishment of the well dispersed nanosheet structure. As shown in Fig. S4, as the amount of oxalic acid added gradually increases from 0.92 g to 1.82 g, the morphology of the product evolves from microrods to the mixture of microrods and nanosheets, and eventually to well disperse nanosheets. XRD patterns in Fig. S4g indicate that monoclinic $NH_4V_4O_{10}$ phase gradually formed with the decrease of triclinic $(NH_4)_6V_{10}O_{28}$ (JCPDS No. 82–0481) phase. Further increase of oxalic acid from 1.82 g to 2.52 g, the formed nanosheets grew up, and then gathered into large blocks. XRD results show that $NH_4V_4O_{10}$ gradually decreased and formed the mixture of VO_2 (JCPDS No. 81–2392) and V_3O_7 (JCPDS No. 27–0940) phase. The formation of the nanosheet structure at the concentration of oxalic acid between 1.52 g and 1.82 g might be due to the appropriate electrical attraction and hydrogen bonding interaction between the nanosheets which lead to their self-assembly to minimize the total surface energy [39]. Ultimately, the $NH_4V_4O_{10}$ nanosheets were decomposed and oxidized into unique mesoporous V_2O_5 nanosheets by the calcination process, corresponding to the following equation.

$$4NH_4V_4O_{10} + O_2 \xrightarrow{400^{\circ}C} 8V_2O_5 + 4NH_3\uparrow + 2H_2O \tag{2}$$

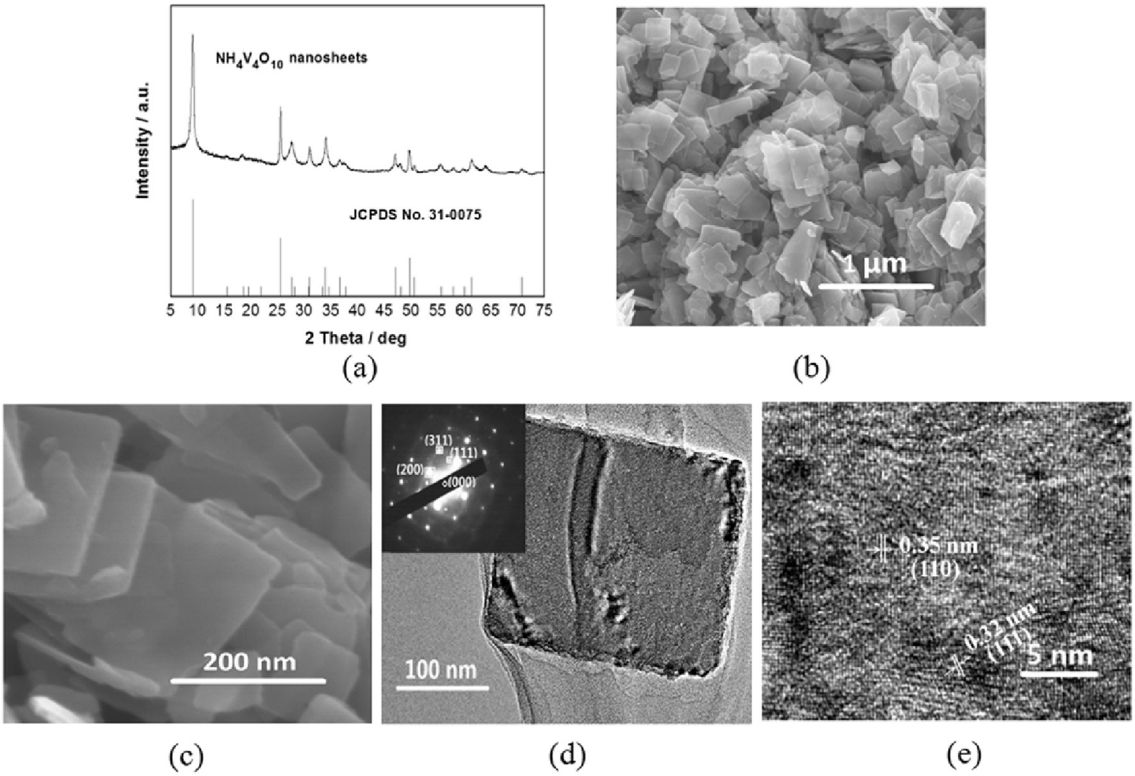

Fig. 2. Characterization of $NH_4V_4O_{10}$ nanosheets. (a) XRD patterns. (b and c) Typical FESEM images with different magnifications. (d) TEM image and the corresponding SAED pattern (inset). (e) HRTEM image.

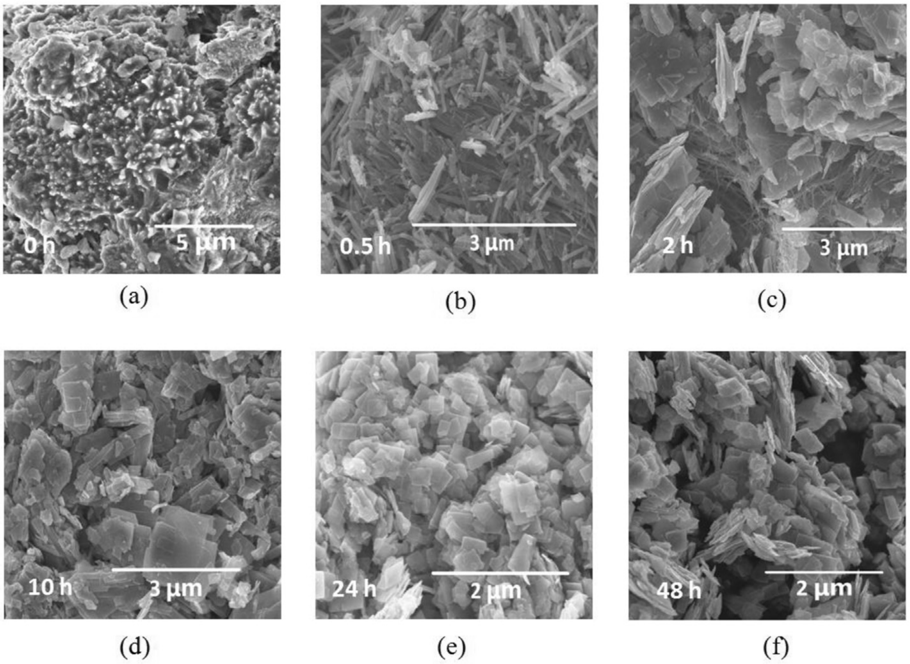

Fig. 3. FE-SEM images of the intermediate compounds after different reaction time (a: 0 h; b: 0.5 h; c: 2 h; d: 10 h; e: 24 h; f: 48 h).

During the conversion from $NH_4V_4O_{10}$ to its corresponding oxides, the internally born ammonia (NH_3) release, and the vanadium oxide layers firstly block the gas release and then are broken by the ammonia sealed inside, at the same time, small void/pores are formed. Numerous such processes concurrently/continuously take place from the outer to inner part of the nanosheets until $NH_4V_4O_{10}$ is completely converted to mesoporous V_2O_5 nanosheets [28,46].

The XRD pattern of the calcined product is shown in Fig. 4a, which can be perfectly indexed as the orthorhombic phase V_2O_5 with excellent crystallinity (JCPDS No. 41–1426 , space group:

Pmmn (59), a = 1.1516 nm, b = 0.3566 nm, c = 0.4372 nm) [44,47,48]. The morphology and microstructure of the as-prepared mesoporous V_2O_5 nanosheets are shown in Fig. 4b–d. The FESEM images in Fig. 4b and c presents that the uniform nanosheet structure is essentially preserved during the calcination and solid-phase conversion process and the thickness of the nanosheet has increased to 50–70 nm from about 20 nm for its precursor nanosheet, which agrees well with the AFM image and the corresponding height profiles in Figure S2b, 66.81 nm for the testing sample. The representative TEM image (Fig. 4d) demonstrates that the prepared V_2O_5 nanosheets are composed of porous and layered structure. The HRTEM image taken from the edge of the nanosheet is shown in the lower right inset in Fig. 4d. A lattice fringe of 0.34 nm can be ascribed to the (110) plane of V_2O_5. The SAED (the upper left inset in Fig. 4d) reveals the single-crystalline nature of the V_2O_5 nanosheets. The pores on the surface of V_2O_5 nanosheets have greatly increased the specific surface area though the sizes of the pores are not uniform (from a few nanometers to tens of nanometers), which can be verified by testing the Brunauer–Emmett–Teller (BET) surface area. As shown in Fig. 4e, the prepared V_2O_5 with a nanoscale subunit-assembled nanosheet hierarchical structure gives rise to a BET surface area of 68 $m^2\ g^{-1}$ and a relatively high pore volume of 0.31 $cm^3\ g^{-1}$, the latter mainly being contributed from the mesoporous in V_2O_5 nanosheets. This surface area is much higher than that of its precursor nanosheets ($NH_4V_4O_{10}$, 23 $m^2\ g^{-1}$) and bulk V_2O_5 (3.5 $m^2\ g^{-1}$). The bulk NH_4VO_3 was also calcined at 400 °C, whose BET surface area (12.4 $m^2\ g^{-1}$) and pore volume (0.09 $cm^3\ g^{-1}$) are also lower than the as-prepared V_2O_5 nanosheets. The Barrett–Joyner–Halenda (BJH) desorption results show that the prepared sample contains mesopores with a size peak of 45.0 nm, which is bigger than that of its precursor (29.5 nm). The confirmation of the oxidation state of vanadium in the prepared V_2O_5 nanosheets was carried out by X-ray photoelectron spectroscopy (XPS) analysis. The high resolution XPS of V 2p after fitting is shown in Fig. 4f. The peaks at 517.53 and 525.05 eV, which are attributed to the spin–orbit splitting of the components, correspond to V^{5+} 2p3/2 and V^{5+}2p 1/2 [49]. It is noteworthy that the V^{4+} peaks are also found at 516.36 eV (V^{4+} 2p3/2) and 523.80 eV (V^{4+} 2p1/2) [50], indicating that the formation of low valence state vanadium. The relative atomic ratio of V^{5+} and V^{4+} is 9:1 calculated based on the peak areas. In order to compensate the charge, the oxygen vacancies must be created in the lattice of V_2O_5 [51] and the formula of the vanadium oxide can be determined to be $V_2O_{4.9}(V_{\ddot{O}})_{0.1}$, which is agreement with the elemental composition results by energy dispersive spectroscopy (EDS) measurement.

To demonstrate the possible structural advantages, the as-obtained mesoporous V_2O_5 nanosheets were evaluated according to their lithium storage performance as a cathode material for LIBs. Fig. 5a shows the first five consecutive cyclic voltammograms (CV) of the novel V_2O_5 mesoporous nanosheets at a scan rate of 0.2 mV s^{-1} in the potential range from 2.5 to 4.0 V. The two main cathodic peaks appear at 3.34 and 3.14 V, suggesting that the two step interaction of the first lithium ion into V_2O_5 and the phase transformations from α-V_2O_5 to ε-$Li_{0.5}V_2O_5$ and δ-LiV_2O_5. These processes can be expressed in equations (3) and (4), respectively.

$$V_2O_5 + 0.5\ Li^+ + 0.5e^- = \varepsilon - Li_{0.5}V_2O_5 \tag{3}$$

$$\varepsilon - Li_{0.5}V_2O_5 + 0.5\ Li^+ + 0.5e^- = \delta - LiV_2O_5 \tag{4}$$

The two anodic peaks appear at 3.32 and 3.48 V corresponding to the lithium de-intercalation and the opposite phase transformation to the cathodic reaction. Besides these peaks, one obvious peak at 3.27 V is observed in the anodic scan, which can be largely attributed to the novel mesoporous-nanosheet-structures. As shown in Fig. 4d, the mesoporous in nanosheets and the space between nanosheets are clearly observed, which facilitate the electrolyte penetration and reduce the energy barrier for Li^+ intercalation/de-intercalation. Therefore, the phase change can happen rapidly. The CV curves

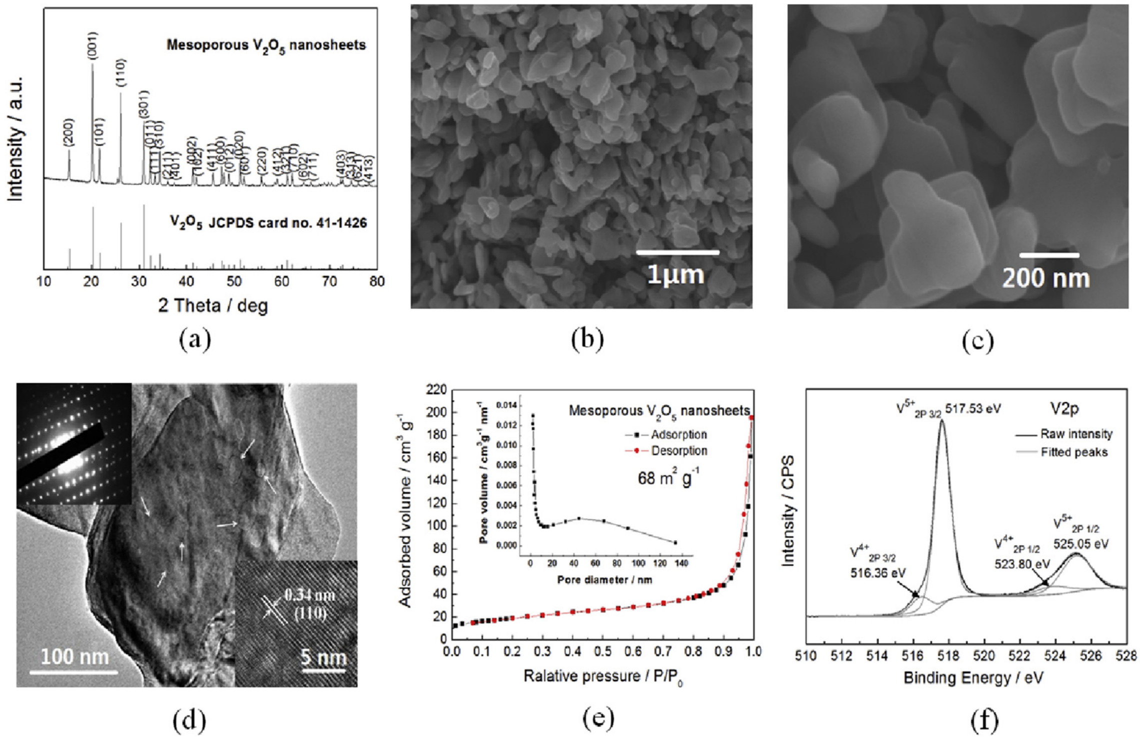

(a) (b) (c)
(d) (e) (f)

Fig. 4. (a) XRD pattern, (b and c) FESEM images, (d) TEM, HRTEM (the lower right inset in d) images and the corresponding SAED (the upper left inset in d), (e) N_2 adsorption/desorption isotherm and the corresponding BJH pore-size distribution curves (inset) and (f) XPS spectra of V 2p of the prepared mesoporous V_2O_5 nanosheets.

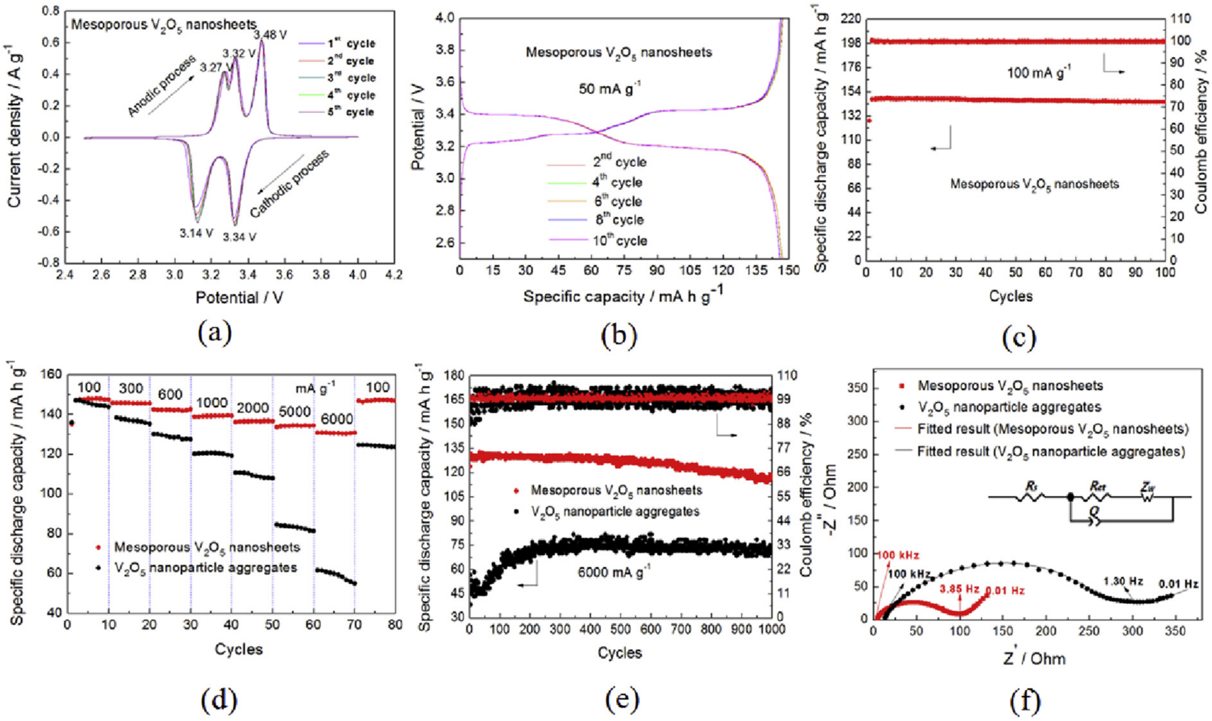

Fig. 5. (a) The first five consecutive CVs of the mesoporous V_2O_5 nanosheets at a scan rate of 0.2 mV s^{-1}. (b) Discharge-charge voltage profiles of the mesoporous V_2O_5 nanosheets at a current density of 50 mA g^{-1}. (c) Cycling performance and Coulombic efficiency of the mesoporous V_2O_5 nanosheets at 100 mA g^{-1}. (d) Rate capability of mesoporous V_2O_5 nanosheets and V_2O_5 nanoparticle aggregates at various current rates. (e) Cycling performance and Coulombic efficiency of the mesoporous V_2O_5 nanosheets and V_2O_5 nanoparticle aggregates at 6000 mA g^{-1}. (f) Comparable Nyquist plots at fully charged stage. Inset: A simplified equivalent circuit. R_s: ohmic resistance of solution and electrodes; R_{ct}: charge transfer resistance; Q: double layer capacitance; Z_w: Warburg impedance.

become almost identical after two cycles, which means a good reversibility of the lithium insertion/extraction process. Fig. 5b shows representative discharge-charge voltage profiles of mesoporous V_2O_5 nanosheet electrode at a current density of 50 mA g^{-1}. Two plateaus are clearly observed at 3.34, 3.14 V on the discharge curves and three plateaus are seen at 3.27, 3.32 and 3.48 V on the charge curves, respectively. It is worthy noted that the discharge-charge curves overlapped well upon cycling, indicating the good reversibility of the electrochemical processes. These discharge/charge profiles are quite consistent with the CV results. The cycling performance of mesoporous V_2O_5 nanosheet electrode is presented in Fig. 5c. At 100 mA g^{-1}, the discharge capacity of mesoporous V_2O_5 nanosheet electrode is 147 mA h g^{-1} at the 2nd cycle, equal to the theoretical capacity for the formation of δ-LiV_2O_5, and still retains a remarkable reversible capacity of 144 mA h g^{-1} at the end of the 100th cycle, corresponding to 98% of the initial capacity (the 2nd cycle). The Coulombic efficiency maintains at more than 99% over all the 100 cycles. Such high Coulombic efficiencies indicate a good reversibility between the discharge and charge processes. The rate capability of mesoporous V_2O_5 nanosheet electrode was evaluated at various current densities, ranging from 100 to 6000 mA g^{-1}, within a potential window of 2.5–4.0 V. For comparison, the rate capability of V_2O_5 nanoparticle aggregates obtained from calcining NH_4VO_3 at 400 °C is also tested under the same conditions. Obviously, the V_2O_5 nanosheets exhibit a high 2nd cycle capacity of 147 mA h g^{-1} at a current density of 100 mA g^{-1} and slightly reduce to 145, 142, 139, 136, 134, and 130 mA h g^{-1} at 300, 600, 1000, 2000, 5000, and 6000 mA g^{-1}. However, the V_2O_5 nanoparticle aggregate electrode is only able to show a discharge capacity of 60 mA h g^{-1} at 6000 mA g^{-1} though its first two cycle discharge capacities at 100 mA g^{-1} are almost the same as V_2O_5 nanosheets does. After the high rate measurement, a capacity of 146 mA h g^{-1} can be obtained for the V_2O_5 nanosheet electrode when the current density returns to 100 mA g^{-1} at the 71st cycle. In addition, the cycling performances of V_2O_5 nanosheet and V_2O_5 nanoparticle aggregate cathodes at high rate of 6000 mA g^{-1} are shown in Fig. 5e. The discharge capacity is 129 mA h g^{-1} at the 2nd cycle for V_2O_5 nanosheet electrode and no obvious capacity fading can be observed in the following cycles. It is noted that even after 1000 cycles, the novel V_2O_5 nanosheet electrode still deliver a high capacity of above 118 mA h g^{-1}, corresponding to 91% of the initial capacity. At the same time, a nearly 99% Coulombic efficiency can be achieved throughout the overall cycling test. While for V_2O_5 nanoparticle aggregate cathode, the 2nd cycle discharge capacity is 38 mA h g^{-1} and the capacity at the 1000th cycle is only 72 mA h g^{-1} though the discharge capacity has some increases in the subsequent cycles. The Coulombic efficiency change range (the change of Coulombic efficiency between minimum value and maximum value) of V_2O_5 nanoparticle aggregate cathode is larger than that of V_2O_5 nanosheet electrode, suggesting the poor high rate reversibility during discharge/charge processes for V_2O_5 nanoparticle aggregate cathode. All of these results indicate that the V_2O_5 nanosheet electrode possesses excellent Li^+ storage performance, superior cyclability and good reversibility at high power rate. A comparison of the electrochemical performance of our mesoporous V_2O_5 nanosheet with some representative reported V_2O_5 nanostructure materials is given in Table S2. To our knowledge, such outstanding cycling stability at 6000 mA g^{-1} in the voltage range of 2.5–4.0 V is the best report up to date [22,28,47,52,53], which can be mainly ascribed to the unique mesoporous V_2O_5 nanosheet structure and the introduced tetravalent vanadium ions and the attendant oxygen vacancies. The influence of this novel structure on the rate capabilities is further verified by the comparison of electrochemical impedance spectra (EIS) results of the prepared mesoporous V_2O_5 nanosheet and V_2O_5 nanoparticle aggregate cathode. The Nyquist plots in Fig. 5f show that the charge transfer resistance (R_{ct}) of V_2O_5 nanosheet electrode is 96.1 Ω, which is much lower than that of V_2O_5 nanoparticle aggregate electrode (302.5 Ω). The remarkably reduced R_{ct} at the electrode/electrolyte interface results from the unique mesoporous nanosheet structure with larger surface area, which increases the contact area between the active sites and electrolytes, and shortens the Li^+ ion diffusion length, thus leads to rapid ion diffusion and an efficient charge transfer. The porous structure of nanosheet is also favorable for accommodating the volume change during discharge/charge processes. Moreover, the oxygen vacancies appeared during the formation process of mesoporous V_2O_5 nanosheets may serve as possible nucleation centers to accelerate phase transformation during Li^+ ion insertion and extraction processes [13,54]. The electrical conductivities of mesoporous V_2O_5 nanosheets and V_2O_5 nanoparticle aggregates were measured by the direct current four-probe technique, which are 2.31×10^{-5} S cm^{-1} and 4.23×10^{-6} S cm^{-1}, respectively. This result suggests an improved electrical conductivity of V_2O_5 nanosheet electrode probably due to the presence of mixed valence state of V^{5+}/V^{4+} [55,56]. The high electrical conductivity plays an important role in the enhancement of the cycling stability and rate capability of the electrode during Li^+ ion insertion/extraction processes.

4. Conclusions

Mesoporous V_2O_5 nanosheets have been successfully synthesized on a large scale by a hydrothermal method followed by instantaneous heating and calcination in air. The as-prepared V_2O_5 nanosheets are composed of several well-defined porous nanosheets that assemble themselves together and form a highly mesoporous nanosheet structure. Such mesoporous nanosheets give rise to high surface area and rich oxygen vacancies, which improved the abilities to buffer the volume variation and transport electron/ion. When applied as a LIB cathode material, the mesoporous V_2O_5 nanosheets display a very high specific capacity of 147 mA h g^{-1} at a current density of 100 mA g^{-1} within the voltage range of 2.5–4.0 V and with relatively stable capacity retention. More importantly, they show an ultra high rate capacity retention capability, with a reversible capacity of 118 mA h g^{-1} after 1000 cycles at 6000 mA g^{-1}. These excellent electrochemical performances suggest that this unique mesoporous V_2O_5 nanosheet is an attractive cathode material for fast charging and high-power LIBs for electric vehicle application.

Acknowledgments

This work was supported by the “thousands talents” program for pioneer researcher and his innovation team, China. This work was also supported by the National Science Foundation of China (51374029), Program for New Century Excellent Talents in University (NCET-13-0668).

Appendix A. Supplementary data

Supplementary data related to this article can be found at http://dx.doi.org/10.1016/j.jpowsour.2015.06.055.

References

[1] Y. Gogotsi, P. Simon, Science 334 (2011) 917.
[2] J. Lee, A. Urban, X. Li, D. Su, G. Hautier, G. Ceder, Science 343 (2014) 519.
[3] S.Y. Lee, K.H. Choi, W.S. Choi, Y.H. Kwon, H.R. Jung, H.C. Shin, J.Y. Kim, Energy Environ. Sci. 6 (2013) 2414.
[4] M. Armand, J.M. Tarascon, Nature 451 (2008) 652.
[5] J.B. Goodenough, Y. Kim, Chem. Mater. 22 (2010) 587.
[6] D. Liu, G. Cao, Energy Environ. Sci. 3 (2010) 1218.
[7] T. Teranishi, Y. Yoshikawa, R. Sakuma, H. Hashimoto, H. Hayashi, A. Kishimoto, T. Fujii, Appl. Phys. Lett. 105 (2014) 238.
[8] L. Zielke, T. Hutzenlaub, D.R. Wheeler, I. Manke, T. Arlt, N. Paust, R. Zengerle, S. Thiele, Adv. Energy Mater. 4 (2014) 156.
[9] J.L. Esbenshade, M.D. Fox, A.A. Gewirth, J. Electrochem. Soc. 162 (2015) A26.
[10] C.W. Ahn, J.J. Choi, J. Ryu, B.-D. Hahn, J.W. Kim, W.H. Yoon, J.H. Choi, D.S. Park, Carbon 82 (2015) 135.
[11] A. Paolella, G. Bertoni, S. Marras, E. Dilena, M. Colombo, M. Prato, A. Riedinger, M. Povia, A. Ansaldo, K. Zaghib, L. Manna, C. George, Nano Lett. 14 (2014) 6828.
[12] C. Delmas, H. Cognacauradou, J.M. Cocciantelli, M. Menetrier, J.P. Doumerc, Solid State Ionics 69 (1994) 257.
[13] Y. Li, J. Yao, E. Uchaker, M. Zhang, J. Tian, X. Liu, G. Cao, J. Phys. Chem. C 117 (2013) 23507.
[14] M.V. Reddy, T.W. Jie, C.J. Jafta, K.I. Ozoemena, M.K. Mathe, A.S. Nair, S.S. Peng, M.S. Idris, G. Balakrishna, F.I. Ezema, B.V.R. Chowdari, Electrochim. Acta 128 (2014) 192.
[15] M.J. Lee, S. Lee, P. Oh, Y. Kim, J. Cho, Nano Lett. 14 (2014) 993.
[16] D. Chao, X. Xia, J. Liu, Z. Fan, C.F. Ng, J. Lin, H. Zhang, Z.X. Shen, H.J. Fan, Adv. Mater. 26 (2014) 5794.
[17] C. Sanchez, R. Morineau, J. Livage, Phys. Status Solidi A 76 (1983) 661.
[18] M. Benmoussa, E. Ibnouelghazi, A. Bennouna, E.L. Ameziane, Thin Solid Films 265 (1995) 22.
[19] H. Yu, X. Rui, H. Tan, J. Chen, X. Huang, C. Xu, W. Liu, D.Y.W. Yu, H.H. Hng, H.E. Hoster, Q. Yan, Nanoscale 5 (2013) 4937.
[20] C. Wu, F. Feng, Y. Xie, Chem. Soc. Rev. 42 (2013) 5157.
[21] M. Castriota, E. Cazzanelli, A. Fasanella, D. Teeters, Thin Solid Films 553 (2014) 127.
[22] A.Q. Pan, H.B. Wu, L. Zhang, X.W. Lou, Energy Environ. Sci. 6 (2013) 1476.
[23] Y. Li, J. Yao, E. Uchaker, J. Yang, Y. Huang, M. Zhang, G. Cao, Adv. Energy Mater. 3 (2013) 1171.
[24] Q. Yue, H. Jiang, Y. Hu, G. Jia, C. Li, Chem. Commun. 50 (2014) 13362.
[25] M.J. Armstrong, D.M. Burke, T. Gabriel, C. O'Regan, C. O'Dwyer, N. Petkov, J.D. Holmes, J. Mater. Chem. A 1 (2013) 12568.
[26] H. Liu, W. Yang, Energy Environ. Sci. 4 (2011) 4000.
[27] X. Rui, Z. Lu, H. Yu, D. Yang, H.H. Hng, T.M. Lim, Q. Yan, Nanoscale 5 (2013) 556.
[28] C. Zhang, Z. Chen, Z. Guo, X.W. Lou, Energy Environ. Sci. 6 (2013) 974.
[29] H. Bai, Z. Liu, D.D. Sun, S.H. Chan, Energy 76 (2014) 607.
[30] Q. An, Q. Wei, L. Mai, J. Fei, X. Xu, Y. Zhao, M. Yan, P. Zhang, S. Huang, Phys. Chem. Chem. Phys. 15 (2013) 16828.
[31] D. Yang, Z. Lu, X. Rui, X. Huang, H. Li, J. Zhu, W. Zhang, Y.M. Lam, H.H. Hng, H. Zhang, Q. Yan, Angew. Chem. Int. Ed. 53 (2014) 9352.
[32] H. Chen, Q. Zhang, J. Wang, Q. Wang, X. Zhou, X. Li, Y. Yang, K. Zhang, Nano Energy 10 (2014) 245.
[33] H.C. Park, K.H. Lee, Y.W. Lee, S.J. Kim, D.M. Kim, M.C. Kim, K.W. Park, J. Power Sources 269 (2014) 534.
[34] X. Yao, J. Kong, D. Zhou, C. Zhao, R. Zhou, X. Lu, Carbon 79 (2014) 493.
[35] P. Samarasingha, D.H. Tran-Nguyen, M. Behm, A. Wijayasinghe, Electrochim. Acta 53 (2008) 7995.
[36] A. Wijayasinghe, B. Bergman, C. Lagergren, Solid State Ionics 177 (2006) 165.
[37] P.N. Trikalitis, V. Petkov, M.G. Kanatzidis, Chem. Mater. 15 (2003) 3337.
[38] G.T. Chandrappa, P. Chithaiah, S. Ashoka, J. Livage, Inorg. Chem. 50 (2011) 7421.
[39] N. Wang, W. Chen, L. Mai, Y. Dai, J. Solid State Chem. 181 (2008) 652.
[40] X.C. Wu, Y.R. Tao, L. Dong, J.M. Hong, J. Mater. Chem. 14 (2004) 901.
[41] V. Petkov, P.N. Trikalitis, E.S. Bozin, S.J.L. Billinge, T. Vogt, M.G. Kanatzidis, J. Am. Chem. Soc. 124 (2002) 10157.
[42] J. Livage, Chem. Mater. 3 (1991) 578.
[43] C. Lausser, H. Coelfen, M. Antonietti, Acs Nano 5 (2011) 107.
[44] Y.S. Hu, X. Liu, J.O. Mueller, R. Schloegl, J. Maier, D.S. Su, Angew. Chem. Int. Ed. 48 (2009) 210.
[45] H. Wang, S. Liu, Y. Ren, W. Wang, A. Tang, Energy Environ. Sci. 5 (2012) 6173.
[46] J. Liu, D. Xue, Adv. Mater. 20 (2008) 2622.
[47] Q. An, P. Zhang, Q. Wei, L. He, F. Xiong, J. Sheng, Q. Wang, L. Mai, J. Mater. Chem. A 2 (2014) 3297.
[48] J. Cheng, B. Wang, H.L. Xin, G. Yang, H. Cai, F. Nie, H. Huang, J. Mater. Chem. A 1 (2013) 10814.
[49] G.A. Sawatzky, D. Post, Phys. Rev. B 20 (1979) 1546.
[50] Y. Feng, Y. Li, F. Hou, J. Power Sources 187 (2009) 224.
[51] Y. Wang, Z. Zhang, Phys. E 43 (2011) 1726.
[52] A. Pan, T. Zhu, H.B. Wu, X. Lou, Chem. -Eur. J. 19 (2013) 493.
[53] Q. Yue, H. Jiang, Y. Hu, G. Jia, C. Li, Chem. Commun. 50 (2014) 13362.
[54] Y. Zhang, P. Xiao, X. Zhou, D. Liu, B.B. Garcia, G. Cao, J. Mater. Chem. 19 (2009) 948.
[55] P. Gomez-Romero, Adv. Mater. 13 (2001) 163.
[56] I. Boyano, M. Bengoechea, I. de Meatza, O. Miguel, I. Cantero, E. Ochoteco, J. Rodriguez, M. Lira-Cantu, P. Gomez-Romero, J. Power Sources 166 (2007) 471.